Engineering Fracture Mechanics 264 (2022) 108357

Contents lists available at ScienceDirect

Engineering Fracture Mechanics

journal homepage: www.elsevier.com/locate/engfracmech

Size effect at aggregate level in microCT scans and DEM simulation – Splitting tensile test of concrete

J. Suchorzewski [a,b,*], M. Nitka [b]

[a] RISE Research Institutes of Sweden, Department of Infrastructure and Concrete Technology, Material Design, Brinellgatan 4, 504 62 Borås, Sweden
[b] Gdańsk University of Technology, Faculty of Civil and Environmental Engineering, 80-233 Gdańsk-Wrzeszcz, Narutowicza 11/12, Poland

ARTICLE INFO

Keywords:
Concrete
Size effect
Splitting test
microCT
DEM

ABSTRACT

The paper describes an experimental and numerical study of size effect on concrete cylindrical specimens in splitting tensile test. Own experimental campaign was performed on specimens with 5 various diameters from $D = 74$, 105, 150, 192 and 250 mm with hardboard loading strips (distributed load according to standard methods) scaled proportionally to the specimen diameter. The crack opening-control system was applied to obtain the post-peak behaviour of all tested specimens including catastrophic behaviour (snap-back). The tested specimens at a certain point were unloaded and scanned with novel high-resolution micro tomography to analyse the macro cracks and phenomena like aggregate breakage, crack branching etc. at the aggregate level. Based on realistic mesostructure the discrete element method (DEM) 2D model of 3 specimens with diameters of $D = 74$, 150 and 250 mm were constructed and tested. The fracture was analysed at macro and micro-level in DEM and directly compared with microCT scans. DEM simulations revealed additional information related to the loss of material strength and ductility with increasing specimen size (size effect). The simulation and experimental results were in good agreement.

1. Introduction

1.1. Size effect

The size effect is an important phenomenon in cementitious composites, which are the most used building materials. With the increase of the element size, the nominal strength (maximum load capacity) and material ductility decrease. Both parameters have significant importance on the engineering construction's safety [1]. This is due to the simplified material properties definitions in common engineering understanding, which do not include phenomena at an aggregate level and lower. In small scale, the concrete specimen exhibits quasi-static response in the post-peak phase, while on in large scale, the post-peak part change into catastrophic snap-back behaviour, due to the sudden drop in strength related to a positive slope in a load–deflection softening branch.

The physical understanding of size effects is of major importance for civil engineers who try to extrapolate experimental outcomes at laboratory scale to actual structures of a practical size. Since large structures are strongly beyond the range of samples tested in laboratories, their design has to rely on a realistic extrapolation of testing results with smaller element sizes and accurate numerical

---

[*] Corresponding author at: RISE Research Institutes of Sweden, Department of Infrastructure and Concrete Technology, Material Design, Brinellgatan 4, 504 62 Borås, Sweden.

E-mail addresses: jan.suchorzewski@ri.se, jan.suchorzewski@pg.edu.pl (J. Suchorzewski), michal.nitka@pg.edu.pl (M. Nitka).

https://doi.org/10.1016/j.engfracmech.2022.108357
Received 15 December 2021; Received in revised form 20 February 2022; Accepted 23 February 2022

models based on the physical phenomena.

Quasi-brittle materials like concrete are subjected to two basic size effect types: (1) statistical (stochastic) and (2) deterministic (energetic) size effect. The nature of the deterministic size effect comes from the intrinsic characteristics of quasi-brittle materials subjected to the fracture process. Damage is initiated at micro-level by the formation of micro-cracks which concentrate in the weakest spot of the material subjected to tensile stress. Micro-cracking causes macroscopic intensive strain volume called fracture process zone (FPZ). When finally discrete crack occurs, the FPZ precedes the macrocrack ahead of its propagation path. The width of FPZ depends on the micro- and meso-structure, thus from the concrete mix design and as the material constant is independent on the specimen size. However, if the samples size increases the remaining elastic part also increases. The proportion of energy dissipated in the FPZ due to fracture and the elastic energy released in the remaining sample volume defines the failure type. If the energy absorbed in FPZ is greater than the elastic energy of the remaining part, which occurs in small samples, the failure is quasi-brittle as certain redistribution of stresses is possible. It also contributes to higher tensile strength. For large specimens, the elastic energy released is greater than the absorption in FPZ and the sample exhibits catastrophically-brittle failure and lower strength [2].

A statistical (stochastic) effect is caused by the spatial variability/randomness of the local material strength and occurs in concrete structures of a positive geometry. The larger size of the concrete member is, the more weak spots occurs [3]. For structures of a practical size, the size effect follows neither the plastic limit load theory nor the linear elastic fracture mechanics. The deterministic size effect is important for moderate size structures. The Weibull statistical size effect has usually a lower impact on nominal strength than deterministic one, moreover, the strength dependence is weaker for small sizes than for large ones and significantly increases as an asymptotic limit for very large size structures [4,5]. In addition, the statistic size effect is caused by strength scatters affecting the local stress fields and therefore, the nominal strength [6–8], which should be taken into consideration. In spite of the sample experimental evidence, the physically based size effect is not taken into account in practical design rules of engineering structures, assuring a specified safety factor with respect to the failure load. Instead, a purely empirical approach is sometimes considered in building codes which is doomed to yield an incorrect formula since physical foundations are lacking. Therefore, the understanding of a size effect is of major importance to ensure the safety of the structure and to optimize the material behaviour.

1.2. *Splitting tensile test*

The splitting tensile (Brazilian) test is the most popular laboratory test on concrete to determine its tensile strength due to loading and specimen shape simplicity. Moreover, for existing structures assessment cylindrical shape specimens are always sampled. This test consists of applying a distributed compressive force along the length of a concrete cylinder, which induces a primarily tensile stress perpendicular to the loading plane of the specimen's cross-section with sharp compressive stress near the points of load application. The splitting tensile strength is generally greater than the direct tensile strength and lower than the flexural strength [9].

Due to rapid damage of the specimen in the displacement control test, the CMOD (crack mouth opening displacement) should be introduced. Thus, the postpeak behaviour of the specimen can be studied. In the Brazilian test, both fracture modes are active (mode I and II), however, mode I one is more significant. Propagation, branching and coalescence of the crack can be captured only if the CMOD is used. The normal components of displacement discontinuity near the crack tip (CTOD-crack tip opening displacement) on the indirect tensile tests are much more important than the shear (CTSD-crack tip sliding displacement) [10–14] due to the nature of the test. That is why this paper will refer to CMOD as only normal components of the crack mouth opening displacement.

It was experimentally proven that a splitting tensile test is subjected to the size effect (on the strength) depending on the cylindrical specimen diameter due to a non-uniform distribution of the tensile stress, caused by compression regions at the loading/supporting points [15–19]. However, to the authors' knowledge, no experimental data was published considering a brittleness increase with increasing diameter in the Brazilian splitting test. Whereas the size effect is characterised by both the strength and ductility reduction with increasing specimen size. Therefore, the own experimental campaign was performed to measure the size effect both on strength and brittleness (see Section 2).

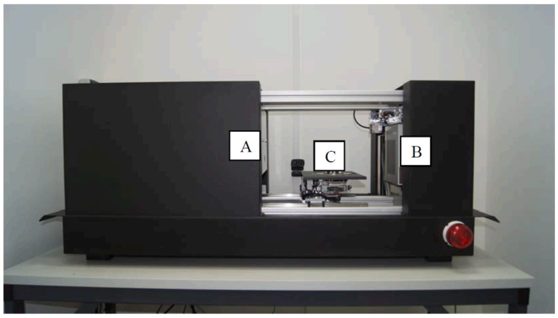

Fig. 1. Overview on X-ray micro-tomograph Skyscan 1173: A) X-ray source, B) flat panel (detector) and C) precision object manipulator (positioning stage) [29].

1.3. Micro-computed tomography

Various methods may be used for fracture analysis of concrete, among them: scanning electron microscopy (SEM) [12], high-speed photography [21], laser speckle interferometry [22], acoustic emission [23], X-ray technique [24,25], Moiré method [26] and Digital Image Correlation (DIC) technique [27].

The x-ray micro-tomography (called briefly micro-CT) is a 3D imaging technique that uses x-rays to create vertical cross-sections of a physical object that is used to reconstruct a virtual 3D model without destroying the original object [28,29]. The micro-CT consists of an x-ray emission gun, rotating stage and flat panel sensitive to x-ray emission detecting the x-ray magnitude. The analysed specimen is being rotated around the vertical axis with a small rotation step. At each step, a 2D black-white image of a specimen with the density map (based on the x-ray absorption) is saved in the computer's memory. To create a 3D image of the specimens' internal structure, a total rotation of 180° is necessary. For specimens with a higher density (large x-ray absorption), the rotation of 360° is used. After that, the 2D image is reconstructed in every horizontal section from individual 2D scans. The reconstructed specimen images may be then rendered and analysed both qualitatively and quantitatively in 3D. The x-ray micro-tomograph Skyscan 1173 represents a new generation in high-resolution desktop X-ray micro-tomography systems (Fig. 1) [24,25,29]. The scans are completed up to ten times faster with the same resolution and image quality as compared to previous micro-CTs with a fixed source-detector design. The scanner was equipped with the newly developed 130 keV microfocus x-ray source with a very stable focal spot position and flat panel sensor of a large format (5 Mpx) with special protection by a lead-glass fibre-optic window. As compared to usual X-ray micro-tomographs, this scanner has two basic advantages: a) large specimens up to 150 mm in diameter may be scanned and b) the specimens are scanned with higher resolution (2–3 μm).

The basic outcome of CT scans is a greyscale image (Fig. 2a) representing the densities of the objects (the whiter is the object, the higher is its density). In the first step, the region of interest must be chosen to pick the area for further analyses (Fig. 2b). Then to distinguish the desired phase (aggregate, cement matrix, pores or crack), a suitable threshold has to be applied, based on density histograms. Choosing high densities, the aggregate may be analysed (Fig. 2c). Finally, aggregate morphology may be quantitatively

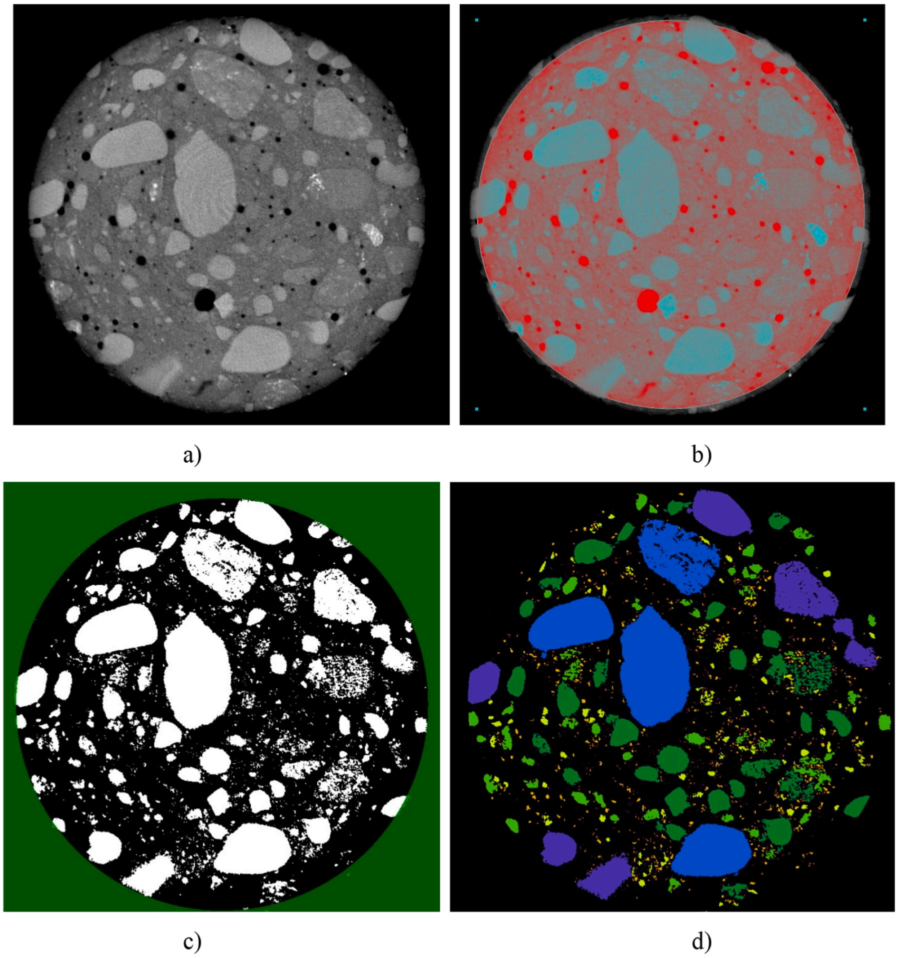

Fig. 2. Mid-section of specimen with diameter $D = 74$ mm: a) original scan image, b-d) region of interest (ROI) for further analyses [30].

measured (Fig. 2d). The parameters as each object surface, volume, porosity (opened and closed pores), the centre of gravity, orientation in 3D, major diameter, sphericity, moments of inertia and many others may be extracted from the micro-CT scans.

1.4. *Aim and scope*

First, the paper describes experimental results of the size effect in the tensile splitting test performed with CMOD-control, which enabled registering concrete's post-peak behaviour and study of the failure type transition typical for size effect, previously observed mainly in flexural and tensile tests [31–33]. Secondly, the microCT analysis of cracks morphology was used to investigate the micro-structural phenomenon affecting the size effect. Last, the discrete element method (DEM) 2D model based on microCT scans with realistic micro-structure was employed to study the fracture process in detail. The DEM model anticipated the size effect both as the strength reduction and the brittleness increase. This article is an extension and supplement to the article by Suchorzewski&Tejchman (2019) [34]. More details and new results with deep analysis are presented here. The focus was laid on the experimental work and tomography scanning results, in contrast with [34], where basic numerical calculations were presented.

2. Experiments

2.1. *Specimens and test procedure*

The presented experimental results have been planned, executed and obtained by the first author as a part of his PhD thesis [30]. The experimental programme on splitting tensile with specimens of the diameter $D = 74$, 100, 150, 192 and 250 mm under the CMOD control was carried out (Fig. 3). The specimens were sawed out from one concrete block with the dimension $200 \times 200 \times 20$ cm^3 after 28 days from casting to obtain results independent of drying shrinkage [35]. After that, the specimens were kept in water until testing after 90 days. The concrete recipe was presented in Table.1. The maximum aggregate diameter was 16 mm. The w/c ratio was equal to 0.53 and the water-binder ration $w/b = 0.44$ with a binder content of 400 kg/m^3 and the sand point of 43.7 % [30].

The specimens were loaded via the hardboard strips with the dimensions: $b = 10$ mm and $t = 4$ mm for $D = 150$ mm (according to the European provisions EN 12390:2012 [36]). For other diameters, the strips width b was proportionally scaled with the diameter (constant ratio $b/D = 0.1$) to exclude the influence of boundary conditions [37,38]. Thus, the vertical load was respectively transferred to the specimen through surface contact and the boundary condition influence was eliminated. The effect of the loading type was investigated in our previous work [34]. The specimens were loaded with static loading machine ZWICK Roell Z400. The machine was equipped with a crack opening extensometer (Sandner EXR10-2x) within the measurement range of ± 2 mm with a maximum error of 2 %. The extensometer base was equal to 40 mm. The extensometer was located at the mid-height of the concrete specimen and glued to the specimen front side. The quasi-static tests were performed under the CMOD-control with the displacement rate of 0.00001 (1×10^{-5}) mm/s. The CMOD-time relationship was perfectly linear in all tests. The CMOD rate was not scaled with the specimen diameter since the loading had a static character.

The specimens' thickness/length was equal to $L = 200$ mm, and as reported in previous works of Carmona et al. (1998) [17] and Lamond (2006) [39] the thickness over 5x$d_{\max}$ (5x16 mm = 80 mm) does not influence the results. Even though, two specimens were tested to double-check the test sensibility for the specimen length. The standard [36] specimen with the length of $L = 300$ mm and shorter specimen $L = 100$ mm with the same standard diameter $D = 150$ mm were tested. Neither the strength, nor the post-peak behaviour was influenced more than 4% due to specimen length (Fig. 4).

2.2. *Results*

The tensile stress versus the normalised crack opening is presented in Fig. 5A. The tensile stresses were calculated from the common formula $\sigma = 2P/(\pi DL)$, where P is a vertical force, D is the diameter of the specimen and L is specimen length. A clear decrease of strength with increasing diameter was observed. Also, the large specimens were more brittle after the peak. The specimen of the diameter $D = 74$ mm reached the average tensile strength of $\sigma = 4.35$ MPa, for $D = 100$ mm - $\sigma = 3.55$ MPa, for the standard diameter D

Fig. 3. The specimens with plywood strips scaled proportionally with specimens' diameter (b/D = const.) [22].

Table 1
Concrete mixture recipe for 1 m^3 [30] (Suchorzewski 2019).

Concrete mixture for 1 m^3			
Ingredient	Type	Amount [%]	Mass [kg]
cement	CEM III 42.5 N		330
water	mixing		176
aggregate	sand 0–2	45	817
	gravel 2–8	25	454
	gravel 8–16	30	545
admixtures	MasterPolyheed219	0,7	1,61
ash EDF			70

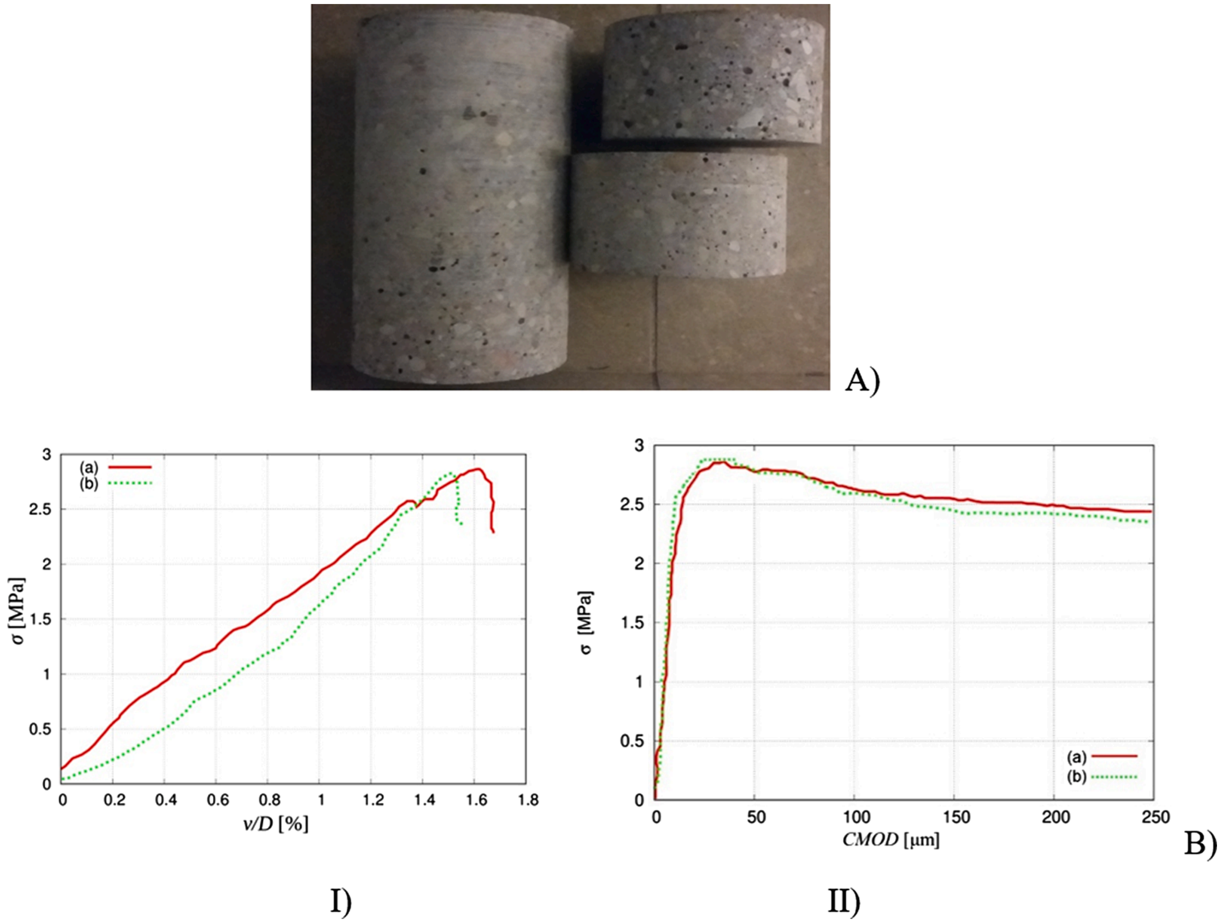

Fig. 4. A) The specimens view and B) tensile stress σ versus I) normalised vertical displacement v/D or II) *CMOD* in splitting tensile test for various specimen length: a) $L = 100$ mm and b) $L = 300$ mm.

$= 150$ mm - $\sigma = 3.22$ MPa, for $D = 192$ mm - $\sigma = 2.80$ MPa and for the largest diameter $D = 250$ mm - $\sigma = 2.65$ MPa.

Fig. 5B presents the evolution of the tensile stress σ versus the normalized vertical displacement v/D for the different specimen diameters. The results' scatter concerning the strength and post-peak behaviour decreased with increasing specimen diameter D. Apart from the decreasing strength, the brittleness increased significantly in the softening part of the curve. For the specimens $D = 74$ mm and $D = 100$ mm, it was characterised by the increasing displacement after the peak while for $D = 150$ mm, $D = 192$ mm and $D = 250$ mm, by the decreasing displacement after the peak (snap-back).

The crack patterns after full failure are shown in Fig. 6 for all tested specimens' diameters after failure. For the specimen $D = 74$ mm with a higher peak load, the crack had two branches dividing a central part of the specimen from the other two halves (Fig. 6A left). For the second specimen with the same diameter, no wedges were observed under supports, however, a secondary crack occurred at the right top of the specimen at the circumference (Fig. 6A right). For the rest of the specimens, a single crack occurred with characteristic wedges under loading/supporting strips. The larger diameter of the specimen was, the less the curvature of the crack appeared.

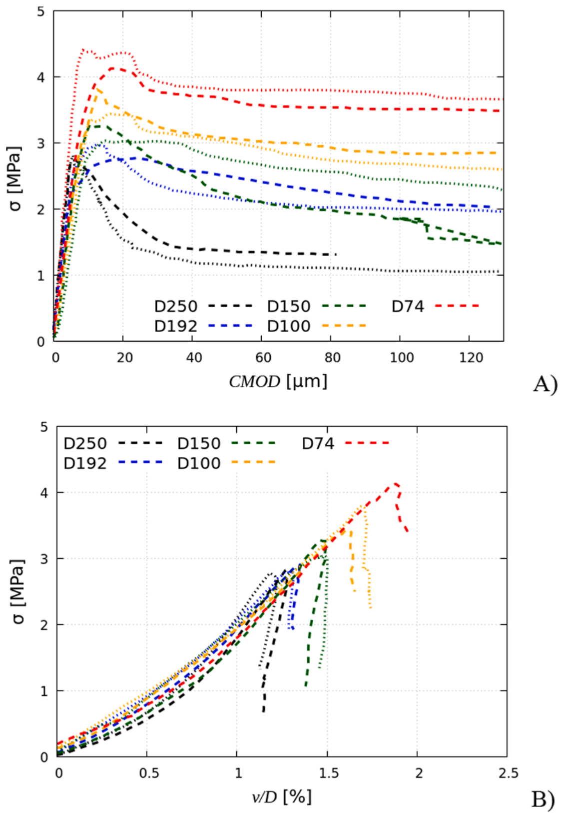

Fig. 5. Tensile stress σ versus: A) *CMOD* and B) v/D in splitting tensile tests with various specimen diameter D ($D = 250$ mm – black lines, $D = 192$ mm – blue lines, $D = 150$ mm – green lines, $D = 100$ mm – orange lines, $D = 74$ mm – red lines) [30,40].

(Fig. 6).

2.3. Micro-CT scans of fracture

The specimen with the diameter of $D = 74$ mm was scanned with micro-CT before loading. Three specimens with diameters $D = 74$ mm, $D = 150$ mm and $D = 250$ mm were chosen for scanning after loading until CMOD = 200 μm (the end of the test). The crack morphologies depending on the specimen diameter were analysed qualitatively and quantitatively.

All concrete specimens were scanned with the same parameters' settings. The X-ray source voltage of the micro-CT scanner was set to 130 keV, the current was 61 μA and the exposure time was equal 2000 ms. The pixel size of the micro-CT was 39.68 μm. The X-ray projections were recorded with the rotation increment of 0.2° within 180°. To reduce the noise in the captured X-ray projections, the frame averaging option was set to be 4 and the random movement option was 10. The scanning time was approximately 8 and 16 h for $D = 74$ mm and $D = 150$ and 250 mm. This was due to an oversize scan for larger specimens, which required double scanning at two different heights.

The basic three phases of concrete were determined from 3D micro-CT images (Fig. 7a): aggregate (Fig. 7b), cement matrix (Fig. 7c) and air voids (Fig. 7d). Moreover, the aggregate size distribution and pore structure were analysed for $D = 74$ mm. The segmentation was performed with the CTAn 1.17.7.2 software delivered by SkyScan Bruker (the producer of the micro-tomograph). The bottom and top thresholds used for each phase were: 0–63 (pores and cracks), 63–112 (cement matrix) and 112–255 (aggregate). After thresholding, fine particles "despeckle" was used to remove artefacts finer than 10 voxels (in volume) except pores.

The crack surfaces of all specimens were segmented and the cracks' volumes were determined. Some cracks were connected with inner pores during fracture which increased their volume. The cracks are presented in Fig. 8 with the marked thickness. The top and bottom of the crack correspond to the loading points. The image was segmented in CTAn and exported to CTvox in 4 files representing each structure thickness (red $w \geq 0.2$ mm, green 0.2 mm $> w \geq 0.1$ mm and blue 0.1 mm $> w \geq 0.05$ mm). It was extremely difficult to segment cracks finer than

0.05 mm (50 μm) since they were close to the used image resolution. The higher thickness of the crack for specimen $D = 74$ mm was clearly visible as the red colour dominated over the others in almost the entire specimen (Fig. 8a). The crack in the specimen $D = 150$ mm was typical for splitting tension with the largest width in the specimen mid-height. Clear wedges both at the specimen top and bottom occurred (Fig. 8b). Those wedges where pieces of the concrete split from the rest of the specimens were excluded from the volume analysis. In specimen $D = 250$ mm, the crack width was non-uniform with a high crack opening at the 3/4 height and a wide

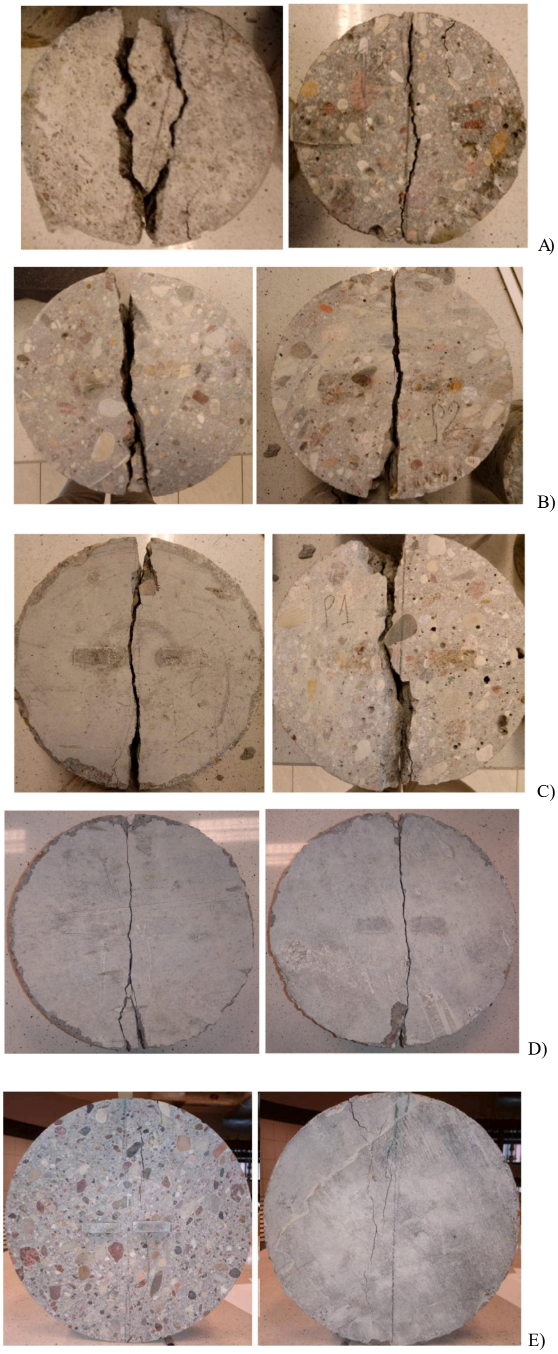

Fig. 6. The crack patterns for specimens' diameters A) $D = 74$ mm, B) $D = 100$ mm, C) $D = 150$ mm, D) $D = 192$ mm and E) $D = 250$ mm for each tested specimen.

opening on the front side (Fig. 8c).

For specimen $D = 74$ mm, the main crack was curved the most of all specimens (Fig. 8a). This conclusion was drawn from experience and observation of the CT image, it was not evaluated quantitatively. The crack did not crush aggregate particles, which indicates that the aggregate had significantly higher strength than the cementitious matrix. The total crack volume was $V = 117.10$ mm^3 and the average crack width was $w = 0.19$ mm. The crack in the specimens $D = 150$ mm and $D = 250$ mm was less curved and exhibited typical wedges at the top and bottom of the specimens, under/over the loading/bearing strips (Fig. 8b-c). The crack volumes were $V = 103.53$ mm^3 and $V = 78.74$ mm^3 and the average crack widths $w = 0.086$ mm and $w = 0.039$ mm for the specimens $D = 150$ mm and $D = 250$ mm, respectively. Moreover, in the specimen $D = 250$ mm, the crack had a few fine branches in the zones ahead of

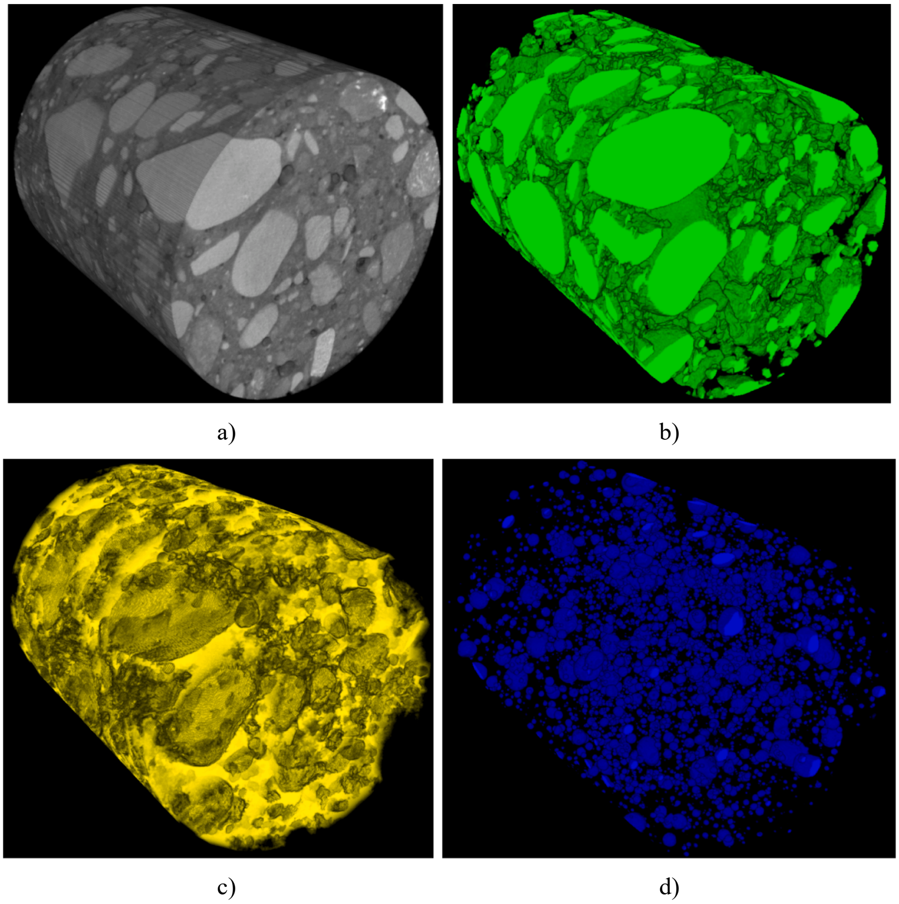

Fig. 7. 3D image of small specimen with diameter of $D = 74$ mm before test: a) original image and visible phases: b) aggregate, c) cement matrix and d) air voids.

wedges (Fig. 8c). The average crack widths are significantly smaller than the value of CMOD at test abortion. CMOD is a global measurement taking into account the crack and elastic deformation of the material around the crack. Secondly, it measures only the maximum crack opening, which is located in the middle, while the crack width varies along the hight of the specimen in the splitting test. It is well-documented phenomenon that cracks tend to close after unloading [41]. A combination of those factors has contributed to a lower average crack width than the maximum crack width at the moment of test abortion.

The crack volume and average crack width decreased with increasing specimen diameter. It was since the crack for small specimen the crack opening was more uniform throughout the whole height of the specimen and had a relatively longer propagation path (was more curved), while for larger specimens the crack was finer at the top and bottom and very straight (relatively shorter propagation path). It could also be related to the unloading of the large specimens with negative displacement slope which caused less damage out of the main fracture zone and enabled partial crack closing after complete unloading for scanning. In the specimens with $D > 74$ mm, the crack intersected 6 ($D = 150$ mm) and 11 aggregate particles ($D = 250$ mm).

2.4. Size effect

During the experimental campaign, the clear size effect occurred with respect to strength and brittleness (Figs. 5 and 9). The strength decreased the most for small specimens from $\sigma = 4.35$ MPa ($D = 74$ mm) to $\sigma = 3.55$ MPa ($D = 100$ mm), so by nearly 20 %. The strength drop was the smallest for the largest specimens (by only 5 % between $D = 192$ mm and $D = 250$ mm). The brittleness was defined for purpose of this study as the angle α between the horizontal axis located at the peak-load level and the softening branch of the stress–strain curve in a clockwise direction. The relation of brittleness to the diameter was opposite with a very similar trend (Fig. 5), however the angle α changed by 9 % (between $D = 74$ mm and $D = 100$ mm) and 5 % (between $D = 192$ mm and $D = 250$ mm) (Fig. 9B).

The results of own experiments on splitting tension were compared with the size effect law by Bazant's (SEL type I for unnotched specimens) [5]. The parameters of the size effect were calibrated with regression at the point $D = 150$ mm and corresponding mean strength of $f_t = 3.13$ MPa: $B = 5.40$ and $D_0 = 5.39$ (Fig. 9A). The experimental results were in good agreement with the theoretical

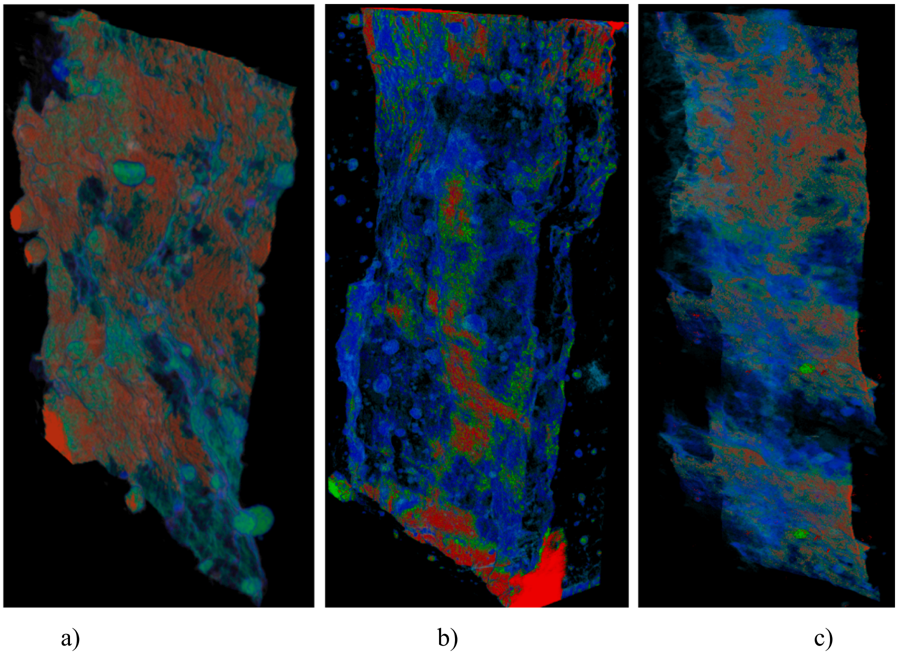

Fig. 8. 3D images of crack for specimens: a) $D = 74$ mm, b) $D = 150$ mm and c) $D = 250$ mm after test with the crack width represents by colours: red $w \geq 0.2$ mm, green 0.2 mm $> w \geq 0.1$ mm and blue 0.1 mm $> w \geq 0.05$ mm) [30] . Please note that the cracks are presented in different scales due to magnification.

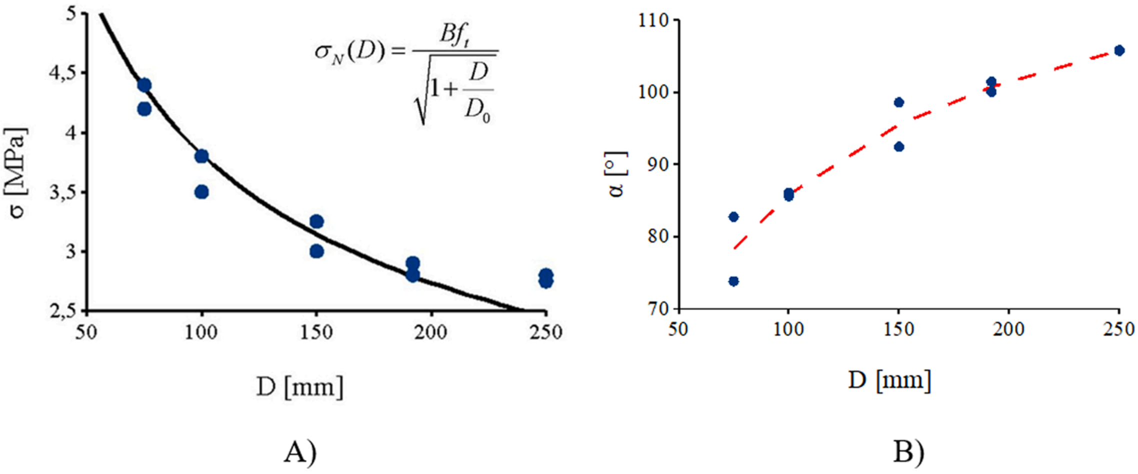

Fig. 9. A) Comparison between experiments and SEL type I by Bažant [5]: tensile strength σ versus specimen diameter D (blue dots – own experiments) [30,40] and B) softening parameter α versus specimen diameter D (dots) and mean value trend (dashed line).

solution ($R^2 = 0.698$) except for the largest specimen $D = 250$ mm, where the strength's reduction in relation to the previous samples size $D = 192$ mm, was smaller by 30 % than the one predicted by SEL.

3. Numerical calculations

3.1. Formulation of discrete element method (DEM) for concrete

The DEM calculations were performed with the three-dimensional spherical discrete element code YADE, which was developed at the University of Grenoble [42,43]. DEM considers a material as consisting of particles interacting with each other through a contact law and Newton's 2nd law via an explicit time-stepping scheme. Outstanding advantages of DEM include its ability to explicitly handle the modelling of particle-scale properties including size and shape which play an important role in the concrete fracture behaviour

[44–50]. The disadvantage is a huge computational cost. The DEM model was successfully used for describing the behaviour of granular materials by taking shear localization into account [51–57]. It also demonstrated its usefulness for both local and global fracture simulations in concrete [40,45–50]. Our DEM calculations for concrete evidently exhibited that it was of major importance to consider both the shape and place of aggregate particles, specimen macro-porosity and strength and number of interfacial transitional zones (ITZs) for realistic reproduction of discrete macro-cracks [40,45–50]. ITZs due to a porous structure acted as an attractor for macro-cracks (created by bridging interfacial micro-cracks) and thus controlled both the concrete strength and brittleness [40,45–50,58].

The 3D spherical discrete element method takes advantage of the so-called soft-particle approach (i.e. the model allows for particle deformation that is modelled as an overlap of particles). A linear normal contact model under compression was used. The interaction force vector representing the action between two spherical discrete elements in contact was decomposed into the normal and tangential components. A cohesive bond was assumed at the grain contacts exhibiting brittle failure under the critical normal tensile load. The tensile failure initiated contact separation and the shear cohesion failure initiated contact slip and sliding obeying the Coulomb friction law under normal compression. The linear elastic response was assumed before reaching the fracture condition (Fig. 10). The contact forces were linked to the displacements through the normal and tangential stiffness moduli K_n and K_s [42,43]. The model can be briefly described by the following equations:

$$\vec{F}_n = K_n U \vec{N} \quad \text{and} \quad \vec{F}_s = \vec{F}_{s,\text{prev}} + K_s \Delta \vec{X}_s \tag{1}$$

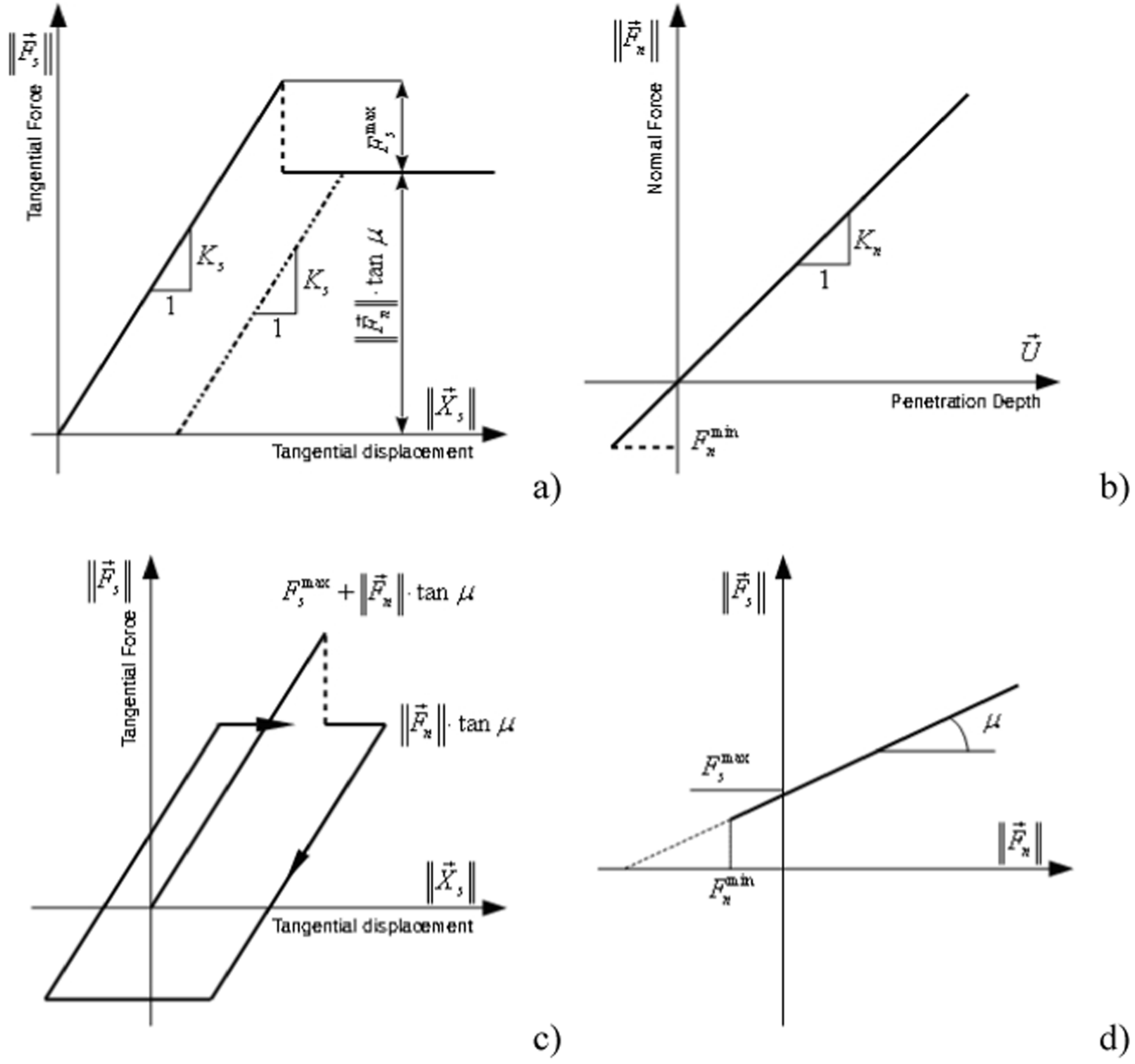

Fig. 10. Mechanical response of DEM: a) tangential contact model, b) normal contact model, c) loading and unloading path in tangential contact model and d) modified Mohr-Coulomb model [45]

$$K_n = E_c\frac{2R_AR_B}{R_A + R_B} \text{ and } K_s = \nu_c E_c\frac{2R_AR_B}{R_A + R_B} \tag{2}$$

$$\|\overrightarrow{F}_s\| - F^s_{\max} - \|\overrightarrow{F}_n\| \times \tan\mu \leq 0 \quad (\text{before contact breakage}) \quad \text{or}$$

$$\|\overrightarrow{F}_s\| - \|\overrightarrow{F}_n\| \times \tan\mu \leq 0 \quad (\text{after contact breakage}) \tag{3}$$

$$F^s_{\max} = CR^2 \text{ and } F^n_{\min} = TR^2 \tag{4}$$

where U is the overlap between elements, $\overrightarrow{N}$ denotes the unit normal vector at the contact point, $\Delta\overrightarrow{X}_s$ is the increment of the relative tangential displacement and $\overrightarrow{F}_{s,\text{prev}}$ is the tangential force from the previous iteration, E_c denotes the modulus of the contact elasticity and υ_c correspond to the normal/tangential stiffens ratio (R_A and R_B are the spheres' radii), μ denotes the inter-particle friction angle and $F^s_{\max}$ and $F^n_{\min}$ corresponds to the critical cohesive and maximum tensile forces, respectively (C is maximum shear stress at the pressure equal to zero and T is maximum tensile normal stress). $F^n_{\min}$ has a negative sign since it denotes the maximum tensile forces (tensile strength) of the contact. There is no limitation in compression (in positive sign) (Fig. 10b, d).

The crack was considered as open if cohesive forces between grains (Eq. (4)) disappeared after reaching the critical threshold. A choice of a very simple constitutive law was intended to capture on average various contact possibilities in real concrete. The structural softening in calculations is solely due to fracture. More details can be found in [45–50].

Five main local material parameters were needed for our discrete simulations: E_c, υ_c, μ, C and T. In general, the DEM material constants are calibrated with the aid of laboratory test results on concrete (e.g. uniaxial tension, uniaxial compression) due to the current data lack on mechanical properties of plain mortar specimens with different initial porosity. The calibration process consists in running test simulations on a given assembly of discrete elements simulating concrete with the same material constants to reproduce the experimental mechanical behaviour [45,48].

3.2. DEM input data

The section describes the input data assumed for 2D DEM calculations of a concrete splitting test. The 3D simulations are obviously more realistic than the 2D ones with respect to the fracture pattern [47,49], however, the 2D analyses may be also useful as a means for studying several different relationships [48]. The differences between 2D and 3D DEM simulations for fractured concrete were found to be minimal at the peak load [47]. Thus, the 2D results at the peak are equal to the 3D results. Those differences increased with growing post-peak deformation when assuming the same material parameters [49]. However, when the 2D DEM model is properly calibrated for concrete based on simple laboratory tests (uniaxial compression, uniaxial tension) it may be used for obtaining realistic results of fracture and a post-peak stress–strain response [34,46]. In addition, the 2D analyses significantly shorten the computation time of DEM simulations. Besides, the splitting laboratory test is usually identified as a typical 2D boundary value problem, i.e. the effect of the specimen length on the crack geometry is assumed to be negligible.

The concrete specimen was described in DEM computations as a four-phase material, composed of aggregate, cement matrix, interfacial transitional zones (ITZs) and macro-voids with the same location, shape and content of aggregates and macro-voids as in the experiment. In the experiments, the minimum aggregate diameter was $d_{\min} = 2$ mm, the maximum aggregate diameter was $d_{\max} = 16$ mm and the mean aggregate diameter $d_{50} = 5$ mm. The aggregate volumetric content was 47.8 %. The total particle volumetric content (sand and aggregate) in concrete was 75 %. The volume of all voids was p = 3.8 % and the volume of voids with the equivalent diameter $d_p < 1$ mm was p = 1.4 % based on micro-CT. The experimentally measured width of ITZs was 20–50 µm [58]. The experimental porosity of ITZs changed between 25 % (at aggregates) down to 1.6 % (cement matrix), based on the image binarization technique [58]. In 2D calculations, the specimen length L included one row of aggregate and mortar particles. In order to construct the real aggregate shape (2 mm $\leq d \leq$ 16 mm) in 2D calculations based on images of the microCT scans mid-sections, the clusters composed of spheres with the diameter of $d = 0.5$ mm connected to each other as rigid bodies were used. Based on experiments, all aggregate grains with the diameter in the range of 2 mm $\leq d \leq$ 16 mm included ITZs. ITZs were simulated for the sake of simplicity as contacts between aggregate and cement matrix grains and thus they had no physical width. The cement matrix was modelled by spheres with the diameter range 0.15 mm $\leq d_{cm} <$ 2.0 mm without ITZs. The specimen preparation process consisted of two stages. Initially, aggregate particles and clusters simulating macro-voids were created. Later, smaller particles were added until the final specimen was filled in 98.6 % by particles in order to realistically model the experimental concrete micro-porosity of 1.4 % (the micro-pores were assumed as the pores with the diameter $d_p < 1$ mm) [40]. Next, all contact forces due to the particle penetration U were deleted. In order to take the starting configuration, the initial overlap was always subtracted in each calculation step when determining the normal forces ($\overrightarrow{F}_n = K_n(U_n - U_0)\overrightarrow{N}$, where U_o - the initial overlap and U_n - the overlap in the calculation n-steps). The grain size distribution curve was the same as in the experiment (with ${d_{cm}}^{\min} = 0.15$ mm). The macro-voids ($d_p \geq 1$ mm) were modelled as empty regions with a real shape and location (after the cement matrix was created, the particles at the place of macro-voids were removed). The initial stresses in concrete due to shrinkage were not considered since the experimental specimens were carefully prepared to avoid drying.

The effect of the different ratios of T_{ITZ}/T_{cm} and C_{ITZ}/C_{cm}, different intergranular friction angle μ in ITZs and different minimum particle diameter in the cement matrix ${d_{cm}}^{\min}$ was comprehensively discussed in [34] and [48]. The calculations [48] showed that if ${d_{cm}}^{\min}$ was small enough (e.g. ${d_{cm}}^{\min} = 0.35$ mm), its effect might be neglected in concrete specimens composed of a sufficiently large

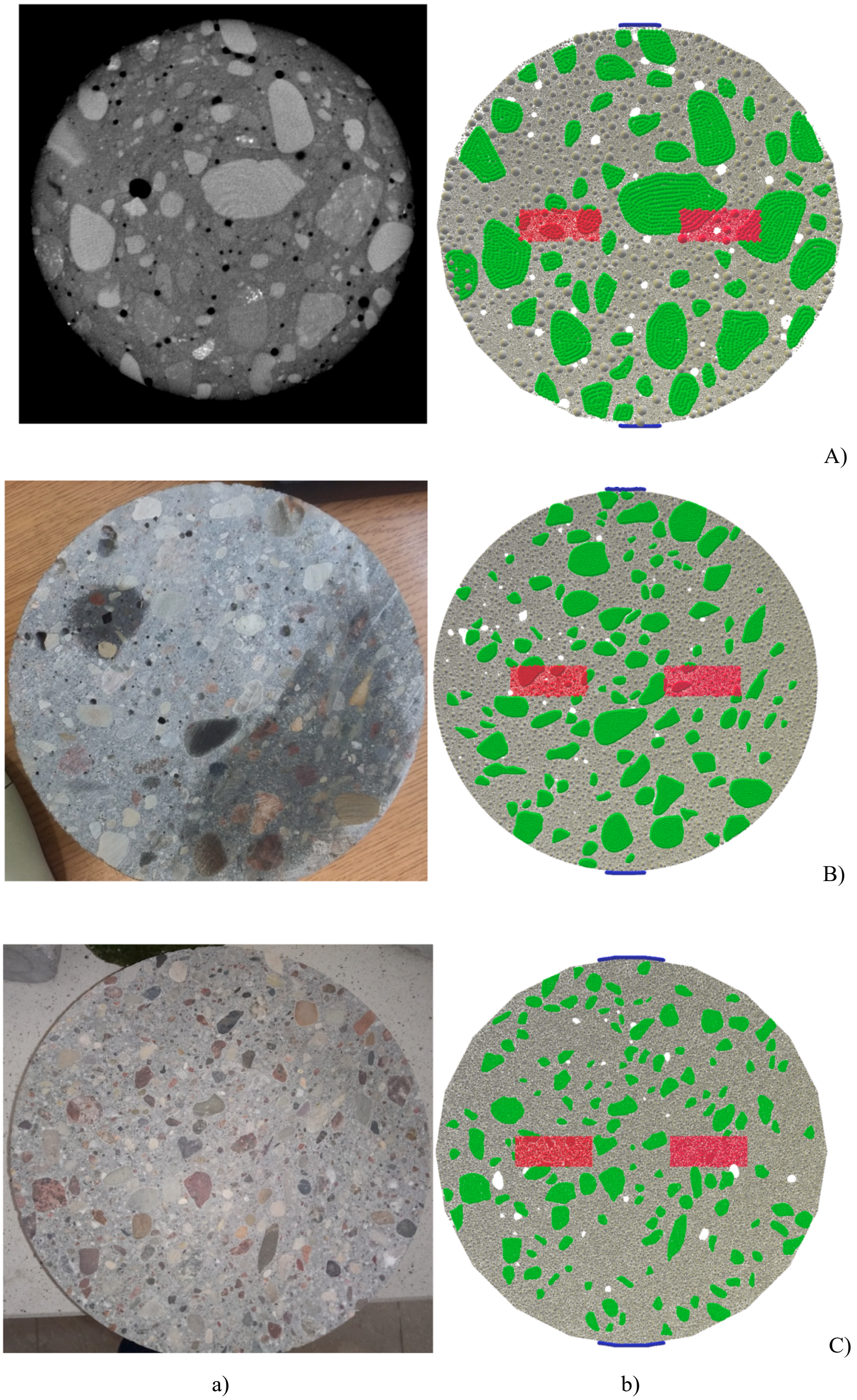

Fig. 11. Concrete specimens a) view on front surface and b) DEM model for 3 different specimen diameters *D*: A) $D = 74$ mm, B) $D = 150$ mm and C) $D = 250$ mm (green particles represent aggregate, grey particles stand for cement matrix and white spots are empty zones representing macro-pores, red squares indicate area for measurement of average *CMOD* and blue particles are loading strips).

number of discrete elements.

3.3. Comparison with own experiments

The laboratory experiments described in Section 2 were simulated with DEM based on the experimental data. The size, shape and position of the aggregate have a significant influence on the micro- (fragmentation and crack path) and macro- (stress–strain curve, especially in peak and post peak behaviour) results [49]. The precise distribution of aggregates was taken into account due to micro-CT images for three specimen diameters $D = 74$ mm, $D = 150$ mm and $D = 250$ mm (Fig. 11). The full 3D CT scan was possible before the test solely for the smallest specimen $D = 74$ mm due to size limitations in the micro-CT system and relatively high concrete attenuation.

The DEM calculations for concrete splitting were carried out with the following parameters of the cohesion and tensile strength: cement matrix ($E_{c,cm} = 15$ GPa, $C_{cm} = 140$ MPa and $T_{cm} = 22$ MPa) and ITZs ($E_{c,ITZ} = 12$ GPa, $C_{ITZ} = 112$ MPa and $T_{ITZ} = 17.6$ MPa) based on uniaxial compression test calibration (Fig. 12) and previous calculations [34,45–50]. ITZs were assumed as the weakest phase. The ratio $E_{c,ITZ}/E_{c,cm} = 0.8$ was chosen based on the experiments by Xiao et al. [59]. The remaining ratios were also assumed as 0.8: $C_{ITZ}/C_{cm} = 0.8$ and $T_{ITZ}/T_{cm} = 0.8$. The hardboard loading/bearing strips at the top and bottom of the specimen were built of spheres' clusters (always the same number of elements, thus the radius of spheres were changed) with the width, proportionally to the diameter D as in experiments. Their diameter was 0.5 mm (for $D = 75$ mm and scaled up for other diameters) with a 5-times lower stiffness than the cement matrix (stiffness of hardboard used in experiments). The deformation was induced by prescribing the vertical top displacement in such a way that the changes of CMOD (crack mouth opening displacement) were approximately linear (as in experiments). CMOD was calculated as a horizontal displacement at the specimen mid-height between mid-points of two regions with the area of $A = 5 \times 15$ mm^2 ($D = 150$ mm), twice as small and twice as large for $D = 74$ mm and $D = 250$ mm. The mid-points were at the distance of 40 mm as in the experiment, for $D = 150$ mm and were proportionally scaled for other diameters. The time step was $\Delta t = 10^{-8}$ s. The calculation time on 8-core CPU 3.3 GHz varied between 10 days and 2 months depending on the specimen diameter. The calculated mean nominal inertial number I for the maximum vertical load (that quantifies the significance of dynamic effects) was $< 10^{-4}$ that always corresponding to a quasi-static regime. The minimum diameter of particles creating the cement matrix was reduced to $d_{min} = 0.15$ mm for all specimens. The 2D concrete specimens under tensile splitting included in total about 42,000, 230,000 and 491,000 spheres for $D = 74$ mm, $D = 150$ mm and $D = 250$ mm respectively. The values of cohesion were calibrated with the aid of the uniaxial compression test wherein random spheres were assumed with the same size as in the concrete mix. The specimens for the compression test were sawed out from the same concrete block as the ones used in splitting tension. The cylindrical specimens had a diameter $D = 100$ mm and a depth of $t = 100$ mm. Therefore, the obtained strength might be directly compared with the one measured on cubic specimens 150 × 150 × 150 mm^2 [60]. The experimental compressive strength was 38 MPa for $\varepsilon = 0.19$ %. A satisfactory agreement both in stiffness and strength was achieved (Fig. 12).

The DEM results for splitting as compared to the experiments are shown in Fig. 13. Very good agreement was achieved between numerical and experimental results for all specimens' diameters with respect to the stress-displacement curve (Fig. 13) and fracture geometry (Fig. 16). Please note that some samples have a slight pre-load (defined in experiments as 1 kN) which in DEM sample $D = 150$ mm is related to the adjustment of loading strips performed numerically. The plywood strips were also not calibrated accurately in numerical calculations (stiffens was overestimated), which has a slight influence on the smaller specimens (especially on the peak slopes).

The calculated maximum tensile splitting stress $\sigma = 2P_{max}/(\pi DL)$ decreased with increasing diameter D. For $D = 74$ mm, the calculated tensile splitting strength was $f_t = 4.0$ MPa for $v/D = 1.8$ %, for $D = 150$ mm, $f_t = 3.2$ MPa for $v/D = 1.5$ % and $f_t = 2.8$ MPa for $v/D = 1.2$ % for $D = 250$ mm (Fig. 13). Apart from the smallest specimen $D = 74$ mm, where the DEM strength was smaller by 4 % than the lower experimental result (Fig. 13 black colour), the remaining DEM results were between the experimental curves. For the specimen $D = 250$ mm, the strength obtained with DEM was equal to the higher experimental result (Fig. 13 red colour). The elastic response of the DEM model was similar as in the experiment, however, the initial hardboard compression-hardening response was not well reproduced (since the loading boards in DEM were assumed to be rigid). This behaviour is clearly visible in the case of the largest

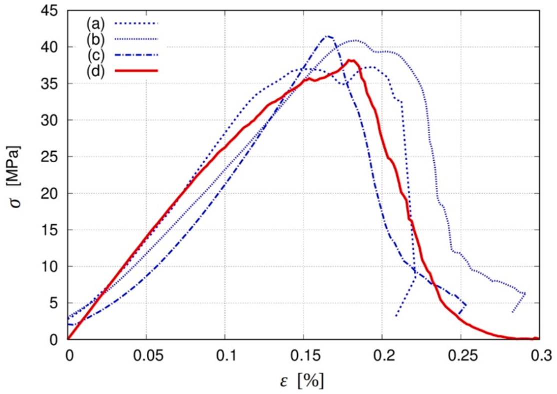

Fig. 12. Stress–strain curves σ-ε curves in uniaxial compression test: a)-c) experimental curves and d) DEM result.

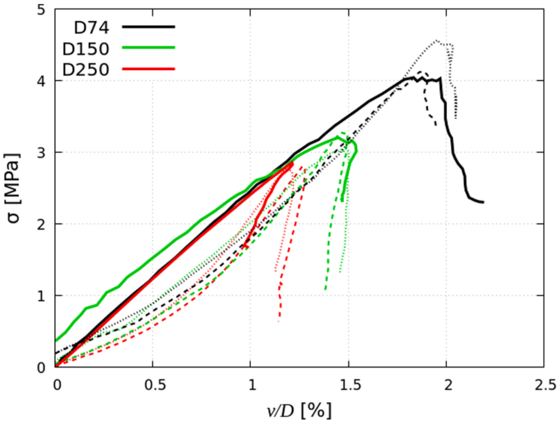

Fig. 13. Tensile stress σ versus normalized displacement v/D for splitting tension: $D = 74$ mm (black lines), $D = 150$ mm (green lines) and $D = 250$ mm (red lines) (DEM – solid line, experiment – dotted lines) [30,40].

specimen (Fig. 13 red colour) where this effect was most significant due to a very high compression force in the experiment (above 80 kN). The concrete brittleness decreased with increasing specimen diameter. A clear snap-back mode of failure occurred for specimens $D > 74$ mm, expressed by a simultaneous reduction of the vertical stress σ and vertical piston displacement v after the maximum stress σ_{max}. The calculated rate of softening was similar as in the experiment for the specimens $D = 74$ mm and $D = 150$ mm. For the largest specimen $D = 250$ mm, the calculated softening was higher than in the experiment.

The clear size effect was obtained in calculations, characterized by the loss of strength and ductility with increasing specimen diameter (Fig. 14). The calculated elastic stiffness was similar for all 3 specimens. The curve for $D = 74$ mm (Fig. 14a) showed a plastic behaviour close to the peak (for $v/D = 1.8$–2 %). The specimen $D = 250$ mm indicated a very brittle behaviour (snap-back) after the peak, changing the displacement direction from positive to negative one (Fig. 14c).

Fig. 15 presents the number of contacts normalised by the number of particles (the so-called coordination number N). The initial coordination number was similar for all specimens and was equal to about $N = 4.82$. In the smallest specimen $D = 74$ mm, the coordination number decreased down to $N = 4.7$, whereas for the specimen $D = 150$ mm and $D = 290$ mm to $N = 4.75$ and $N = 4.78$. From the peak load to the test end, the reduction rate of N was higher for the smaller specimen due to a more intense fracture related to the specimen area.

Finally, the crack morphologies expressed by deformed specimens were compared with the micro-CT scans (Fig. 16).

For the specimen $D = 74$ mm (Fig. 16A), the crack propagated close to the same aggregate particles, however, on their opposite sides than in the experiment. The crack propagated near the large aggregate in the specimen's mid-height on the right side instead of breaking it on the left side. The bottom part of the crack was narrow and straight as in the experiment, however, the crack propagated on the left side of a large aggregate, opposite to the experiment wherein it followed the right edge of the aggregate (Fig. 16Ab). Additionally, the crack was more curved. Also, the large aggregate at the mid-height of the specimen was broken in the experiment. The top of the specimen was crushed in the experiment that was reproduced in DEM as intensive micro-cracking of the cement matrix under the loading board (Fig. 16Aa) and wider crack opening. In the small specimen, some fine differences in the aggregate shape and pores' position greatly influenced the crack pattern. Moreover, the 3D aggregate arrangement influenced the crack shape. To obtain more realistic crack patterns, 3D DEM simulations should be carried out. The cracks computed in DEM for $D = 150$ mm were more

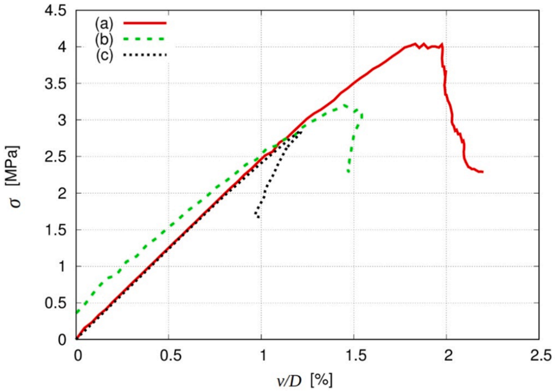

Fig. 14. Tensile stress σ versus normalized displacement v/D curves for splitting in DEM for specimen diameters D: a) $D = 74$ mm, b) $D = 150$ mm and c) $D = 250$ mm.

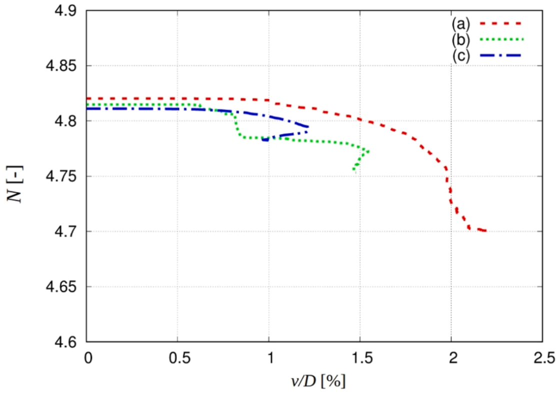

Fig. 15. Coordination number N versus normalized displacement v/D curves for splitting tension test calculated with DEM in specimens with different diameter D: a) $D = 74$ mm, b) $D = 150$ mm and c) $D = 250$ mm.

realistic as compared to the experiment (Fig. 16B). For $D = 150$ mm, no aggregate breakage occurred in the experiment (Fig. 16Ba). Note that the crushed piece of specimen fell apart during transportation (Fig. 16Ba). The same crack's shape was reproduced in DEM as to the crack's branching at the specimen top (Fig. 16Bb). The main crack followed the left side of a large aggregate in the specimen's mid-height, however, another branching appeared at the specimen bottom (Fig. 16Bb) with a finer crack that propagated at the same side of the aggregate as in the experiment. Finally, the largest specimen $D = 250$ mm was almost symmetrically cracked in DEM while in the experiment it was curved to the right side (Fig. 16Cb), probably due to a small load eccentricity. The crack was curved to the left at the specimen top, both in the experiment and DEM, forming a wedge connecting the straight part of the crack with the loading strip edge (Fig. 16C). Similar behaviour was obtained in the specimen's mid-height wherein the crack in DEM was curved to the left (Fig. 16Cb). Even though, the macro-crack developed along other aggregate particles, it had a very small width in the specimen mid-height and was branched with various micro-cracks at the bottom and top, as in the experiment and DEM (Fig. 16C). The intense cracking at the top and bottom (the wedges) was obtained in the model as a multiple micro cracking in the cement matrix.

The macroscopic DEM results: strength (Fig. 17A) and angle α between the horizontal axis and softening curve (Fig. 6B) from the experiments (Section 2.2) were directly compared with DEM simulation results. The strength reduction was very similar in the experiment and DEM for the specimens $D = 150$ mm and $D = 250$ mm. The size effect on brittleness (defined as the angle α between the horizontal axis and the softening part of the curve) was stronger in DEM than in the experiment. For the smallest specimen, the softening angle in DEM was equal to the mean angle in the experiment ($\alpha = 78^\circ$) whereas for the specimens $D = 150$ mm and $D = 250$ mm was equal to $\alpha = 95^\circ$ and $\alpha = 106^\circ$ in the experiments and $\alpha = 102^\circ$ and $\alpha = 120^\circ$ in the numerical calculations (the difference 7-13 %).

4. Conclusions

The following conclusion may be derived from the presented experimental and numerical results on size effect in concrete at aggregate level:

- An experimental campaign on the tensile splitting test of concrete cylinders with various diameters under CMOD-control exhibited a clear size effect. The ultimate concrete tensile strength decreased by 3 % (between $D = 197$ mm and $D = 250$ mm) and 15 % (between $D = 74$ mm and $D = 100$ mm). In total it decreased by 35 % between the smallest and largest analysed specimen. The decreasing strength loss rate with increasing specimen diameter was in accordance with other studies of Bažant [15] and Hasegawa [16]. The ductility expressed as the post-critical curve inclination angle decreased by 42°, changing the behaviour from quasi-brittle, to catastrophically brittle (snap-back).
- The experimental size effect was realistically reproduced in DEM calculations at the aggregate level, i.e. the concrete strength and ductility decreased with increasing concrete specimen diameter. The calculated decreasing strength approached an asymptote with increasing cylindrical specimen diameter within the considered specimen size range and followed the theoretical solution of Bažant's SEL type I.
- DEM proved its capability to model concrete fracture in detail by taking the snap-back instability into account. The agreement of calculated stress-displacement results and crack shapes with experimental ones was satisfactory.
- The crack volume and average crack width decreased with increasing specimen diameter due to crack branching. This could be one more physical phenomenon related to the size effect.

Future research in this topic could include evaluation of the crack propagation rate in specimens of different sizes by analysis of the DEM results. It might bring additional insights into the size effect.

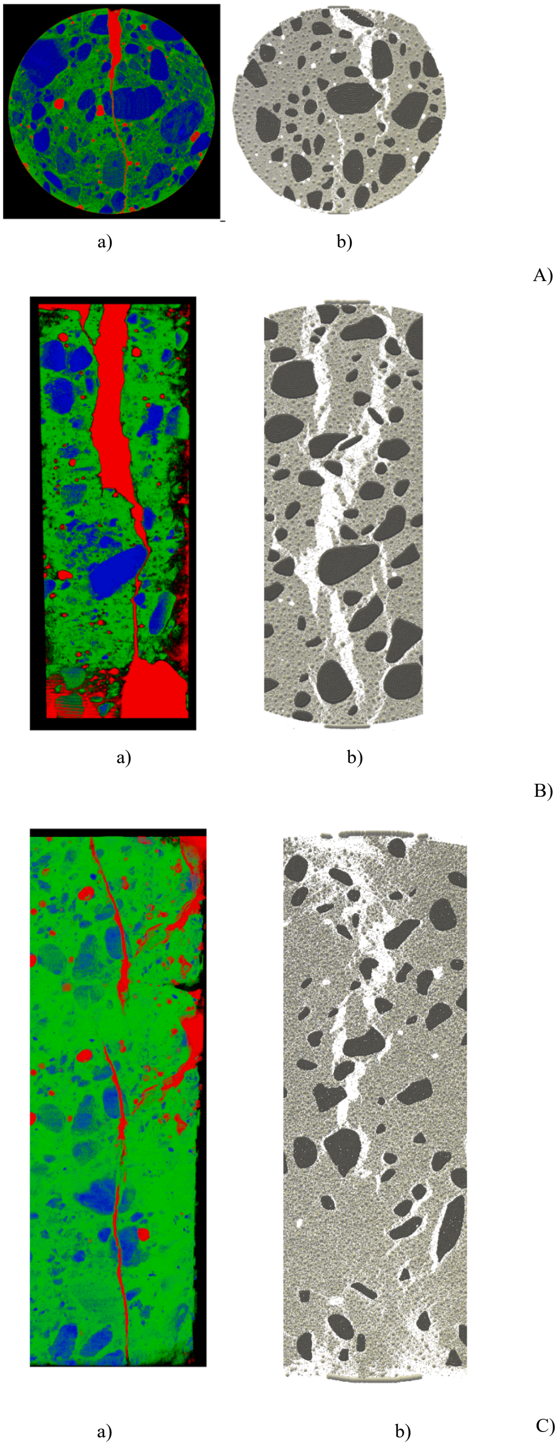

a) b)

A)

a) b)

B)

a) b) C)

Fig. 16. Crack geometry: a) micro-CT images and b) deformed specimens in DEM (multiplied by 50 due to visibility) for different specimen diameters D: A) $D = 74$ mm, B) $D = 150$ mm and C) $D = 250$ mm [30]

CRediT authorship contribution statement

J. Suchorzewski: Conceptualization, Investigation, Methodology, Writing – original draft, Visualization. **M. Nitka:** Methodology, Writing – review & editing.

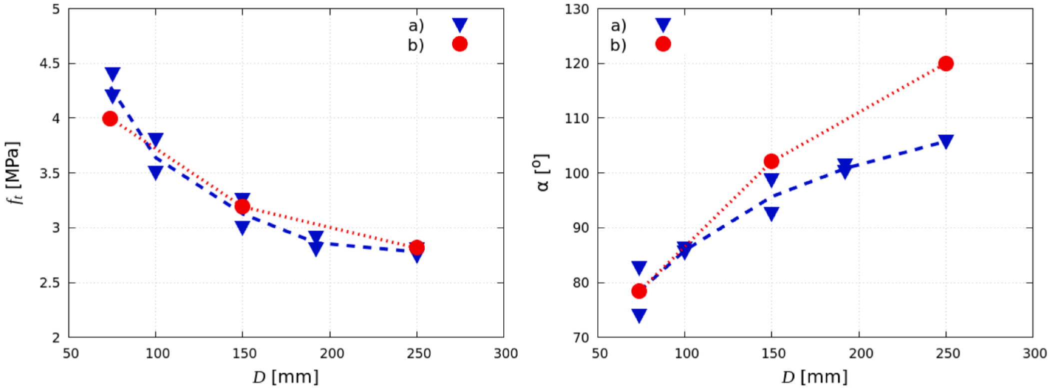

A)

B)

Fig. 17. Comparison of experimental and numerical results of A) tensile splitting strength *ft* and B) softening parameter α against specimen diameter *D* for: a) experimental specimen (blue triangles) and b) DEM result (red dots).

Declaration of Competing Interest

The authors declare that they have no known competing financial interests or personal relationships that could have appeared to influence the work reported in this paper.

Acknowledgements

The research work has been carried out within the project: “*Experimental and numerical analysis of coupled deterministic-statistical size effect in brittle materials*” financed by the National Science Centre NCN (UMO-2013/09/B/ST8/03598) and the project “*The Influence of concrete mesostrucutre on crack initiation and propagation – experiments and multi-scale numerical calculation*” financed by the National Science Centre NCN (UMO-2017/25/B/ST8/02108).

References

[1] Bažant ZP, Planas J. Fracture and size effect in concrete and other quasibrittle materials. CRC Press LCC, Boca Raton; 1998.
[2] Tanabe T-A, Itoh A, Ueda N. Snapback failure analysis for large scale concrete structures and its application to shear capacity study of columns. J Adv Concr Technol 2004;2(3):275–88.
[3] Weibull W. A statistical theory of the strength of materials. Proc Roy Swedish Inst Eng Res 1939;151(1).
[4] Weibull W. A statistical distribution function of wide applicability. J Appl Mech 1951;18(9):293–7.
[5] Bažant ZP. Size effect in blunt fracture: concrete, rock, metal. J Engng Mech 1984;110(4):518–35.
[6] Eliáš J, Vořechovský M. Fracture in random quasibrittle media: I. Discrete meso-scale simulations of load capacity and fracture process zone. *Engng Fract Mech* 2020;235:107160. https://doi.org/10.1016/j.engfracmech.2020.107160.
[7] Vořechovský M, Eliáš J. Fracture in random quasibrittle media: II. Analytical model based on extremes of the averaging process. *Engng Fract Mech* 2020;235: 107155. https://doi.org/10.1016/j.engfracmech.2020.107155.
[8] Eliáš J, Vořechovský M, Skoček J, Bažant ZP. Stochastic discrete meso-scale simulations of concrete fracture: Comparison to experimental data. Eng Fract Mech (Pergamon) 2015;135:1–16. https://doi.org/10.1016/j.engfracmech.2015.01.004.
[9] Balbo JT. Relations between indirect tensile and flexural strengths for dry and plastic concretes. IBRACON Struct Mater J 2013;6(6):854–74.
[10] Marji MF. Simulation of crack coalescence mechanism underneath single and double disc cutters by higher order displacement discontinuity method. J Central South Univ 2015;22(3):1045–54.
[11] Haeri H, Sarfarazi V, Bagher Shemirani A, Marji MF. On the direct experimental measurement of mortar fracture toughness by a compression-to-tensile load transformer (CTLT). Constr Build Mater 2018;181:687–712.
[12] Alizadeh R, Fatehi Marji M, Abdollahipour A, Pourghasemi Sagand M. Development of higher-order displacement discontinuity method to simulate fatigue crack growth in brittle materials. Engng Fract Mech 2021;258:108087. https://doi.org/10.1016/j.engfracmech.2021.108087.
[13] Sarfarazi V, Haeri H, Marji MF, Zhu Z. Fracture mechanism of Brazilian discs with multiple parallel notches using PFC2D. Periodica Polytech Civ Eng 2017;61 (4):653–63.
[14] Fatehi Marji M. Numerical analysis of quasi-static crack branching in brittle solids by a modified displacement discontinuity method. Int J Solids Struct 2014;51 (9):1716–36.
[15] Bažant Z, Kazemi MT, Hasegawa T, Mazars J. Size Effect in Brazilian Split-Cylinder Tests: Measurements and Fracture Analysis. ACI Mater J 1991:325–32.
[16] Hasegawa T, Shioya T, Okada T. Size effect on splitting tensile strength of concrete. Proceedings, Japan Institute 7th Conference 1985:309–12.
[17] Carmona S, Gettu R, Aguado A. Study of the post-peak behaviour of concrete in the splitting-tension test. *Fracture Mechanics of Concrete Structures*, Proceedings FRAMCOS-3, Aedificatio Publishers, D-79104 Freiburg, Germany; 1998, 111-120.
[18] Kadlecek Sr V, Modry S, Kadlecek Jr V. Size effect of test specimens on tensile splitting strength of concrete: general relation. Mater Struct 2002;35:28–34.
[19] Torrent J. A general relation between tensile strength and specimen geometry for concrete - like materials. Mater Struct 1977;10:187–96.
[21] Bhargava J, Rehnström Å. High speed photography for fracture studies of concrete. Cem Concr Res 1975;5(3):239–47.
[22] Jacquot P, Fournier JM. Interferometry in Speckle Light: *Theory and Applications*. Springer, Berlin; 2000.
[23] Maji A, Ouyang C, Shah SP. Fracture mechanisms of concrete based on acoustic emission. J Mater Res 1990;5:206–17.
[24] Skarżyński Ł, Suchorzewski J. Mechanical and fracture properties of concrete reinforced with recycled and industrial steel fibers using Digital Image Correlation technique and X-ray micro computed tomography. Constr Build Mater 2018;183:283–99.

[25] Skarżyński Ł, Marzec I, Tejchman J. Fracture evolution in concrete compressive fatigue experiments based on X-ray micro-CT images. Int J Fatigue 2019;122:256–72.
[26] Ri S, Muramatsu T, Saka M, Nanbara K, Kobayashi D. Accuracy of the Sampling Moiré Method and its Application to Deflection Measurements of Large-Scale Structures. Exp Mech 2012;52:331–40.
[27] Skarżyński Ł, Korol E, Tejchman J. Measurements and calculations of the width of the fracture process zones on the surface of notched concrete beams. J Strain Anal Engng Des 2011;47(1):319–32.
[28] Proudhon H. Using X-ray micro-tomography to probe microstructure and damage of structural materials. WEMESURF contact course; 2010.
[29] Skarzyński Ł, Tejchman J. Experimental investigations of fracture process in concrete by means of x-ray micro-computed tomography. Strain 2016;52:26–45.
[30] Suchorzewski J. Investigations of size effect in concrete at aggregate level - experiments and calculations results using discrete element method. Gdańsk University of Technology; 2019. PhD thesis.
[31] Bažant ZP, Pfeifer P. Determination of fracture energy from size and brittleness number. *ACI Mater J* 1987a;84:463–80.
[32] Le Bellego C, Gérard B, Pijaudier-Cabot G. Chemomechanical effects in mortar beams subjected to water hydrolysis. J Eng Mech ASCE 2000;126:266–72.
[33] Skarżyński Ł, Tejchman J. Modelling the effect of composition on the tensile properties of concrete. *Understanding the tensile properties of concrete* (edited by Jaap Weerheijm). London: Woodhead Publishing Limited; 2013. p. 52–97.
[34] Suchorzewski J, Tejchman J, Nitka M. Experimental and numerical investigations of concrete behaviour at meso-level during quasi-static splitting tension. Theor Appl Fract Mech 2018;96:720–39.
[35] Vorechovsky M. Interplay of size effects in concrete specimens under tension studied via computational stochastic fracture mechanics. Int J Solids Struct 2007;44:2715–31.
[36] EN12390-6:2012 – European standard Testing hardened concrete Part 6: Tensile splitting strength of test specimens, European Committee for Standardization; 2012.
[37] Rocco C, Guinea GV, Planas J, Elices M. Size effect and boundary conditions in the Brazilian test: Experimental verification. Mater Struct 1999;32:210–7.
[38] Rocco C, Guine GV, Planas J, Elices M. Review of the splitting-test standards from a fracture mechanics point of view. Cem Concr Res 2001;31:73–82.
[39] Lamond JF. Significance of tests and properties of concrete and concrete-making materials. *ASTM Int*, Pielert (Eds.), Barr Harbour Drive; 2006.
[40] Suchorzewski J, Tejchman J. Investigations of size effect in concrete during splitting using DEM combined with x-ray micro-CT scans. In: Pijaudier-Cabot G, Grassl P, La Borderie C, editors. 10th International Conference on Fracture Mechanics of Concrete and Concrete Structures FraMCoS-X; 2019.
[41] Skarżyński Ł, Tejchman J. Experimental investigations of damage evolution in concrete during bending by continuous micro-CT scanning. Mater Characterization 2019;154:40–52.
[42] Kozicki J, Donze FV. A new open-source software developer for numerical simulations using discrete modeling methods. Comput Methods Appl Mech Engng 2008;197:4429–43.
[43] Šmilauer V, Chareyre B. Yade DEM Formulation. Manual 2011.
[44] Donze FV, Magnier SA, Daudeville L, et al. Numerical study of compressive behaviour of concrete at high strain rates. J Eng Mech 1999;122(80):1154–63.
[45] Nitka M, Tejchman J. Modelling of concrete behaviour in uniaxial compression and tension with DEM. Granular Matter 2015;17(1):145–64.
[46] Skarżyński L, Nitka M, Tejchman J. Modelling of concrete fracture at aggregate level using FEM and DEM based on x-ray µCT images of internal structure. Engng Fract Mech 2015;10(147):13–35.
[47] Nitka M, Tejchman J. A three-dimensional meso-scale approach to concrete fracture based on combined DEM with x-ray µCT images. Cem Concr Res 2018;107:11–29.
[48] Suchorzewski J, Tejchman J, DEM Nitka M. simulations of fracture in concrete under uniaxial compression based on its real internal structure. Int J Damage Mech 2018;27(4):578–607.
[49] Nitka M, Tejchman J. Comparative DEM calculations of fracture process in concrete considering real angular and artificial spherical aggregates. Eng Fract Mech 2020;239:107309. https://doi.org/10.1016/j.engfracmech.2020.107309.
[50] Suchorzewski J, Tejchman J, Nitka M, Bobiński J. Meso-scale analyses of size effect in brittle materials using DEM. Granular Matter 2019;21(9):1–19.
[51] Nitka M, Tejchman J, Kozicki J, Leśniewska D. analysis of micro-structural events within granular shear zones under passive earth pressure conditions. Granular Matter 2015;17(3):325–43.
[52] Kozicki J, Tejchman J, Mühlhaus H-B. Discrete simulations of a triaxial compression test for sand by DEM. Int J Num Anal Methods Geom 2014;38(18):1923–52.
[53] Danuta L, Nitka M, Tejchman J, Pietrzak M. Contact force network evolution in active earth pressure state of granular materials: photo-elastic tests and DEM, *Granular Matter* 2020:22–71.
[54] Grabowski A, Nitka M, Tejchman J. Micro-modelling of shear localization during quasi-static confined granular flow in silos using DEM. Comput Geotech 2021;134:104108. https://doi.org/10.1016/j.compgeo.2021.104108.
[55] Grabowski A, Nitka M, Tejchman J. Comparative 3D DEM simulations of sand–structure interfaces with similarly shaped clumps versus spheres with contact moments. Acta Geotech 2021;16(11):3533–54.
[56] Grabowski A, Nitka M, Tejchman J. 3D DEM simulations of monotonic interface behaviour between cohesionless sand and rigid wall of different roughness. Acta Geotech 2021;16(4):1001–26.
[57] Nitka M, Grabowski A. Shear band evolution phenomena in direct shear test modelled with DEM. Powder Technol 2021;391:369–84.
[58] Nitka M, Tejchman J. Meso-mechanical modelling of damage in concrete using discrete element method with porous ITZs of defined width around aggregates. Eng Frac Mech 2020;231:107029. https://doi.org/10.1016/j.engfracmech.2020.107029.
[59] Xiao J, Li W, Sun Z, Lange DA, Shah SP. Properties of interfacial transition zones in recycled aggregate concrete tested by nanoindentation. Cem Concr Compos 2013;37:276–92.
[60] EN 12390-3:2019 Testing hardened concrete – Part 3: Compressive strength of test specimens, European Committee for Standardization; 2019.